

This is a repository copy of Evaluation of uncertainty in material flow predictions in hammer forging of steel through constitutive modelling.

White Rose Research Online URL for this paper: <a href="https://eprints.whiterose.ac.uk/id/eprint/232832/">https://eprints.whiterose.ac.uk/id/eprint/232832/</a>

Version: Published Version

## Article:

Koval, O. orcid.org/0009-0006-7719-6058, Das, A. orcid.org/0000-0002-6405-5735, Paramatmuni, C. orcid.org/0000-0001-7069-7331 et al. (2 more authors) (2025) Evaluation of uncertainty in material flow predictions in hammer forging of steel through constitutive modelling. Journal of Manufacturing Processes, 133. pp. 1207-1221. ISSN: 1526-6125

https://doi.org/10.1016/j.jmapro.2024.11.048

## Reuse

This article is distributed under the terms of the Creative Commons Attribution (CC BY) licence. This licence allows you to distribute, remix, tweak, and build upon the work, even commercially, as long as you credit the authors for the original work. More information and the full terms of the licence here: https://creativecommons.org/licenses/

## Takedown

If you consider content in White Rose Research Online to be in breach of UK law, please notify us by emailing eprints@whiterose.ac.uk including the URL of the record and the reason for the withdrawal request.



FISEVIER

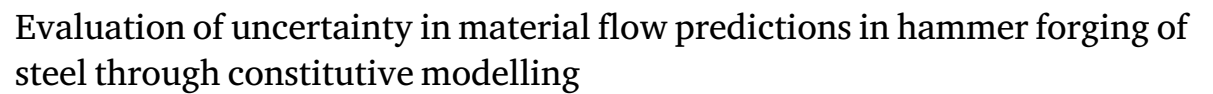
Contents lists available at ScienceDirect

## Journal of Manufacturing Processes

journal homepage: www.elsevier.com/locate/manpro



## Full Length Article



Oleksii Koval <sup>a</sup>, Anindya Das <sup>b</sup>, Chaitanya Paramatmuni <sup>a</sup>, Ed Pickering <sup>b,c</sup>, Daniel Cogswell <sup>a</sup>

- <sup>a</sup> School of Chemical, Materials and Biological Engineering, University of Sheffield, Sheffield, S1 3JD, United Kingdom
- <sup>b</sup> Department of Materials, University of Manchester, Manchester, M13 9PL, United Kingdom
- <sup>c</sup> Henry Royce Institute, Royce Hub Building, Oxford Rd, Manchester, M13 9PL, United Kingdom

## ARTICLE INFO

#### Keywords: Hammer forging Finite element analysis Constitutive modelling Uncertainty quantification Calibration

## ABSTRACT

Reliable modelling of plastic deformation during thermomechanical processing requires robust constitutive models incorporating material and process parameters. This study employs the hyperbolic sine model to predict the strain response of 708M40 steel at elevated temperatures and strain rates. A novel calibration approach comprising three stress-strain datasets derives optimal model parameters that account for uncertainties arising from microstructural heterogeneity. Key parameters, including the activation energy (Q), the strain rate sensitivity (n), the pre-exponential factor (A), and the scaling parameter  $(\alpha)$ , are determined to minimise prediction errors. These parameters are calibrated respectively to 350352 J/mol, 5.9, 1.2 · 1014 s<sup>-1</sup> and 0.0075 MPa-1 to predict peak stress based on the average of three model parameter sets. The confidence in stress predictions increases with temperature and is influenced by a strain rate at high temperatures. This calibrated constitutive model is employed within hammer forging simulations to model previously published experimental studies performed at 1030 °C and 1300 °C under unlubricated conditions. The numerical analysis showed accurate height predictions for blow efficiencies of 50 % and 40 % at 1030 °C and 1300 °C, respectively. Then, the evaluated uncertainties in flow stress were incorporated into hammer forging simulations to study their effect on post-forging predictions. At 40 % efficiency, the model predicts the final height with corresponding uncertainties of  $10.62 \pm 1.46$  mm and  $7.76 \pm 1.54$  mm, while the experimental observations are 9.5 ± 0.2 mm and 7.6 ± 1 mm at 1030 °C and 1300 °C respectively. Further validation against experimental results confirmed that the predicted cross-sectional deformation flow lines closely matched those within the workpiece. A multifactorial experiment with 3600 simulations was performed to study the effect of uncertainties in thermomechanical responses and process conditions on post-forging geometry. This numerical experiment suggest that increased temperature and blow efficiency result in extensive deformation and greater die-metal contact, making further deformation more challenging and reducing the influence of initial flow stress uncertainties. This detailed understanding of the intertwined effect of material and process parameters on the response of steels aims to support the development of efficient computer-aided manufacturing.

## 1. Introduction

Constitutive models play a significant role in simulating metal forming operations. These models establish the connection between stress and strain, serving as a fundamental basis for predicting behaviour of metals during shaping processes. However, development of such models poses a challenge due to the heterogeneous nature of materials, influenced by factors such as process conditions and deformation history [1–3]. In addition, metallic alloys often display non-linear and time-dependent responses, rendering it difficult to incorporate all aspects of material behaviour within a single model. In order to

address these, it is essential to evaluate uncertainties, enabling a more comprehensive and realistic representation of the inherent variability and complexities in material responses. Such evaluation results in more reliable and consistent outputs in forming processes.

The material of interest is 708M40, a low-alloy steel [4], which can possess a combination of phases based on the processing history such as ferrite and pearlite [5,6], ferrite and martensite [1], ferrite and bainite [7], and a combination of ferrite, martensite and retained austenite [2]. These microstructures lead to mechanical properties

E-mail address: o.koval@sheffield.ac.uk (O. Koval).

https://doi.org/10.1016/j.jmapro.2024.11.048

<sup>\*</sup> Corresponding author.

Table 1
Chemical composition of BS970:708M40 steel grade and its analogues.

Country	Grade	C (%)	Si (%)	Mn (%)	P (%)	S (%)	Cr (%)	Mo (%)
UK	708M40	0.36-0.44	0.10-0.40	0.70-1.00	≤0.035	≤0.04	0.9-1.2	0.15-0.25
USA	4140	0.38-0.43	0.15-0.35	0.75-1.00	≤0.035	≤0.04	0.8-1.1	0.15-0.25
EU	42CrMo4	0.38-0.45	≤0.40	0.60-0.90	≤0.035	≤0.035	0.9-1.2	0.15-0.30
	(1.7225)							
Japan	SCM440	0.38-0.43	0.15-0.35	0.60-0.85	≤0.03	≤0.03	0.9-1.2	0.15-0.30

that render the alloy well-suited for applications where resistance to wear and abrasion is essential, providing durability and extending the lifespan of the material [8–10]. The properties are attributed to molybdenum additions providing uniform hardness and high strength, while chromium contributes to the steel's ability to form hard and wear-resistant surfaces [2,11]. Common applications are drive shafts, bolts, gears as well as surface and sub-surface components in oil and gas industries. Since 708M40 is used across diverse sectors, there are various international material equivalents, each designated differently based on the classification system used by individual countries. Equivalent analogues include AISI 4140 [12], 1.7225/42CrMo4 [13] and JIS SCM440 [14] steel grades. The comparison in chemical composition between stated steel grades can be seen in Table 1.

Due to the extensive use of 708M40, numerous studies have focused on creating constitutive models that explain the variation of flow stress in response to deformation conditions. Among notable and established constitutive models are the Zerilli-Armstrong [15], Johnson-Cook [16], Hensel-Spittel model [17], and hyperbolic sine model combined with the Arrhenius equation [18,19]. One notable study among many is the work by Lin et al. [19]. The authors conducted hot compression tests on 42CrMo steel, deriving a constitutive model where the flow stress is as a hyperbolic function of the Zener-Hollomon parameter. Kim et al. [18] modified the Voce's constitutive relations to improve the accuracy of predicting the flow stress behaviour of AISI 4140. The Hensel-Spittel model was used to simulate 42CrMo4 by Venet et al. [20]. This model combines multiple deformation mechanisms into a single equation and can be reduced by setting certain parameters to zero. Venet et al. identified the parameters resulting in a better prediction accuracy for 42CrMo4 compared to those from a standard material database. Although these studies derived optimal model parameters to predict the mechanical behaviour of 708M40, there has been limited focus on assessing the uncertainty in model parameters. This uncertainty arises from experimental measurements and variations in processing history and microstructure, which in turn affect the thermomechanical behaviour of materials.

High-temperature uniaxial responses of metals are typically used to calibrate the constitutive models. These tests are often conducted to a maximum strain rate of 10-50 s<sup>-1</sup> [18-20]. This range covers strain rates observed in mechanical, screw, and hydraulic press operations [21]. However, deformation rates can be even higher in some manufacturing processes, reaching up to 100 s<sup>-1</sup>, which is typical for high-energy rate (drop/hammer) forging processes [21]. This implies that it is not only necessary to calibrate the models against uniaxial high strain rate responses but also to validate them further against high-energy rate manufacturing data to obtain reliable plastic flow of metals. To the authors' knowledge, there are only a handful of studies aiming at the calibration of constitutive models at such elevated strain rates. Among these studies are the works by Zhu et al. [22] and Song and Sanborn [23], where the modified Zerilli-Armstrong and Johnson-Cook constitutive models respectively were deployed to account for thermal softening due to adiabatic temperature rise. While these studies provide great insights and well-calibrated models to understand the plastic flow at high strain rates, their validation for a high-energy rate forging process remains elusive. The current study attempts to close this gap by calibrating and employing the constitutive model to predict material flow during hammer forging.

The outlined constitutive models can be used in conjunction with the finite element method (FEM) based process modelling to improve

the predictability of metal shaping processes by explicitly accounting for the uncertainties in material and process parameters. Formerly, Steden and Trimm [24] studied the sensitivity of Johnson-Cook model parameters in cutting simulations. They used a full factorial test design to conduct and analyse cutting simulations, focusing on the sensitivity of the material and process parameters. Other studies have focused solely on studying the influence of finite element model parameters (e.g. heat transfer coefficient, friction) on simulation outputs. Snape et al. [25] investigated the impact of these parameters in simulations of open-die forging. Their findings revealed that the heat transfer coefficient has a minimal influence on the upsetting forging process. The authors highlighted the crucial role of friction factor, particularly in governing maximum generalised strain due to its impact on shear within the workpiece. Thus, it is evident that the integration of FEM based process modelling tools with well calibrated constitutive models, which account for uncertainties in material and process parameters, are necessary to understand the flow of metals during manufacturing.

This work employs a hyperbolic sine model and introduces a new perspective to calibration of the constitutive model. Unlike previous studies that primarily focused on obtaining one set of model parameters, this research focuses on the use of multiple sources of published stress—strain datasets to obtain the range of responses for 708M40 at varying process conditions. That is, this study not only aims to account for the heterogeneity in the macroscopic responses of steels, which result from variations in local microstructures, but also from variations in test conditions. In addition, the effect of uncertainties in constitutive model parameters on the predicted response of metals is explored in great detail. To the authors' knowledge, such a detailed investigation of uncertainties is lacking in the current literature. Further, these uncertainties are propagated within a commercial finite element package DEFORM to understand their influence on the flow of metal during hammer forging (high strain-rate process).

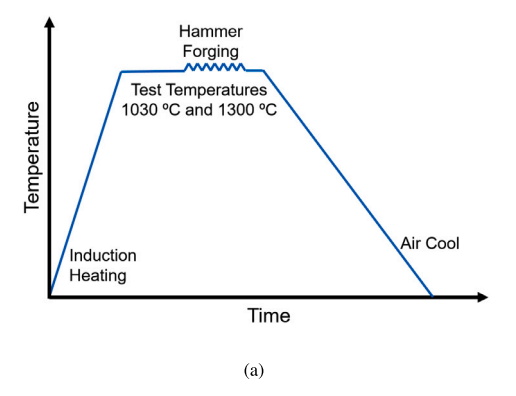
The paper is structured as follows: Section 2 overviews Hill et al.'s hammer forging experiments [26,27], which is the basis for this work. Section 3 details the simulation setup, constitutive model, and calibration. Section 4.1 presents calibrated model parameters, their impact on flow stress predictions, and the role of uncertainties. Section 4.2 discusses the optimal blow efficiency selection, leading to validation of the model against experimental observations. Section 4.3 further analyses the influence of uncertainty on predictions under various process conditions. Section 5 provides a summary of the findings.

## 2. Hammer forging and microstructure characterisation

As this work builds upon hammer forging experiments conducted by Hill et al. [26,27], a brief account of the process parameters and characterisation of the microstructures before and after deformation are detailed in this section.

## 2.1. Hammer forging process

Hill et al. [26,27] conducted hammer forging on 24 ring specimens, using eight different process conditions. These process conditions include two soaking temperatures (1030  $^{\circ}$ C and 1300  $^{\circ}$ C) and four different lubricant variations — unlubricated (U), synthetic water-based lubricant (S), graphite water-based lubricant (G) and graphite—molybdenum disulphide grease (GM). The specimens were extracted



Sample Condition	Trial 1	Trial 2	Trial 3		
1U	125	503			
2U	0	202			
(b)					

Fig. 1. (a) The layouts showing stages in hammer forging process; (b) Top view of the sample distribution. The samples are hammer forged after induction heating at 1030 °C and 1300 °C followed air cooling. The distribution of deformed samples show variations in the deformed geometry, which could be caused by heterogeneity in materials and/or the process parameters. U — unlubricated condition. 1 and 2 refer to 1030 °C and 1300 °C respectively.

from a drawn 708M40 round bar in the hardened and tempered "T" condition, with a hardness range of 248–302 HB. Prior to forging, all cylindrical billets were machined to have an outer diameter of 65 mm, a wall thickness of 16.25 mm and a height of 20 mm.

The schematic representation of the hammer forging process is shown in Fig. 1(a). The billets were heated using the induction method, applying 350 kJ of energy for 6.5 s to heat samples to 1030 °C, and 413 kJ for 7.5 s to reach 1300 °C. While Hill et al. [26,27] examined lubricated and unlubricated conditions, the current research focuses only on the unlubricated condition for simplicity. In addition, the lower flat die was maintained at temperature above 100 °C. Further, the blow energy of the hammer falling under gravitational acceleration was determined to be 21.5 kJ. The process parameters include constant blow energy, fixed initial billet temperature, transfer time from heater to die, dwell time (pre-forging), die temperatures, billet-die friction, convective heat transfer coefficient, and blow efficiency ( $\eta$ ). The blow efficiency is the fraction of total input energy that is available for plastic deformation of the material. It is shown in several studies the blow efficiency ranges between 0.3 and 0.6 for "hard" blows, which finish with a flash after each blow [28-30]. The geometry of the samples after forging at 1030 °C and 1300 °C in unlubricated condition are shown in Fig. 1(b). While U indicates the unlubricated condition, 1 and 2 indicate the temperatures 1030 °C and 1300 °C respectively. The figure shows the considerable variation in the geometry of the deformed samples. For instance, observe the variation in the inner diameters of the samples after hammer forging. This could be caused by the variation in material properties, hammer forging process parameters, or the combination of the two, which is the primary focus of the current article.

## 2.2. Microstructural characterisation

Since the mechanical properties of materials reflect the behaviour of their inherent microstructures, undeformed and forged samples were characterised to understand how the microstructure evolves during hammer forging. The samples for microstructural observation were extracted according to the schematic shown in Fig. 2. Standard metallographic procedures were employed to prepare sample surfaces for observation under microscopes. Sample surfaces were etched using 2% Nital solution to observe under scattered electron (SE) mode in FEI Magellan HR FEG-SEM operating at 5 kV. Unetched surfaces were used for performing electron backscattered diffraction (EBSD) using Tescan Mira LC FEG SEM equipped with an Oxford systems EBSD symmetry detector operating at 20 kV and 27 nA. Fe-BCC phase was indexed using AZtecCrystal Version 4.3 software, where the step size was maintained between 0.1 to 0.3  $\mu m$ . The MTEX toolbox was used to analyse the resulting inverse pole figure (IPF) maps. The as-received material was also observed under the optical microscope to study the microstructure in undeformed condition, which was found to be completely

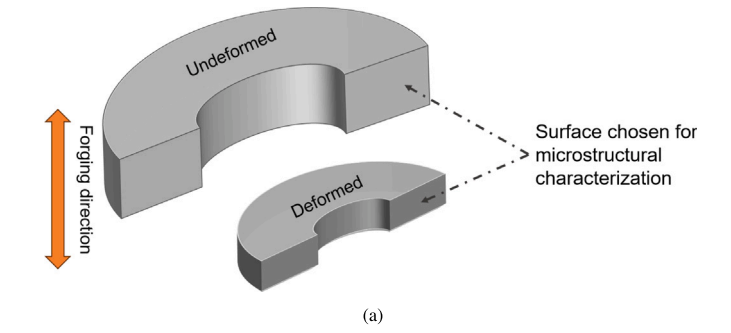


**Fig. 2.** Schematic representation of undeformed and forged 708M40 specimen indicating the surface used for microstructural measurements using electron back-scattered diffraction and scanning electron microscopy.

martensitic in nature, as shown in Fig. 3(a). The undeformed state was also subjected to SEM-EDX mapping, to obtain information about the elemental distribution, which revealed the preferential segregation of Cr and Mn (although mild) throughout the material, as shown in Fig. 3(b), (c) and (d). It can be observed in Fig. 3(b), the vertical bands appearing dark in contrast (as pointed in the figure) are the regions of preferential enrichment by Cr and Mn (Fig. 3(c and d)). However, the segregation of Cr and Mn did not produce any change in the type of phases present in the undeformed material.

The deformed materials were first studied under SEM, in order to investigate the microstructure after forging. Fig. 4 shows the micrographs of the sample forged at 1030 °C. The microstructure show narrow bands of martensite (region 2), as shown in Fig. 4, whereas the rest of the material consist of a mixture of microstructures consistent with upper and lower bainite (region 1). This heterogeneity appears to be due to the aforementioned chemical banding, which already existed in the undeformed material, creating difference in the transformation kinetics upon heat treatment. The chemical banding due to segregation of Mn, Si and Cr aided the banded regions to transform into martensite despite slow cooling, whereas the rest of the area transformed into bainite. These bands that were vertical, straight and parallel to the forging direction before deformation (Fig. 3(b), (c) and (d)) may show distinct distribution after forging driven mainly by local heterogeneous deformation, which is investigated later in detail.

Fig. 5(a) shows the EBSD IPF-Z maps of the undeformed sample, which only consists of martensite. The prior austenite grain size (PAGB) of the undeformed condition was calculated using the parent grain reconstruction method using OI AZtecCrystal software (version 3.1), as mentioned in [31]. The average PAGB size was calculated to be of  $\approx\!30$   $\mu m$ , from the parent grain reconstruction process. The microstructures

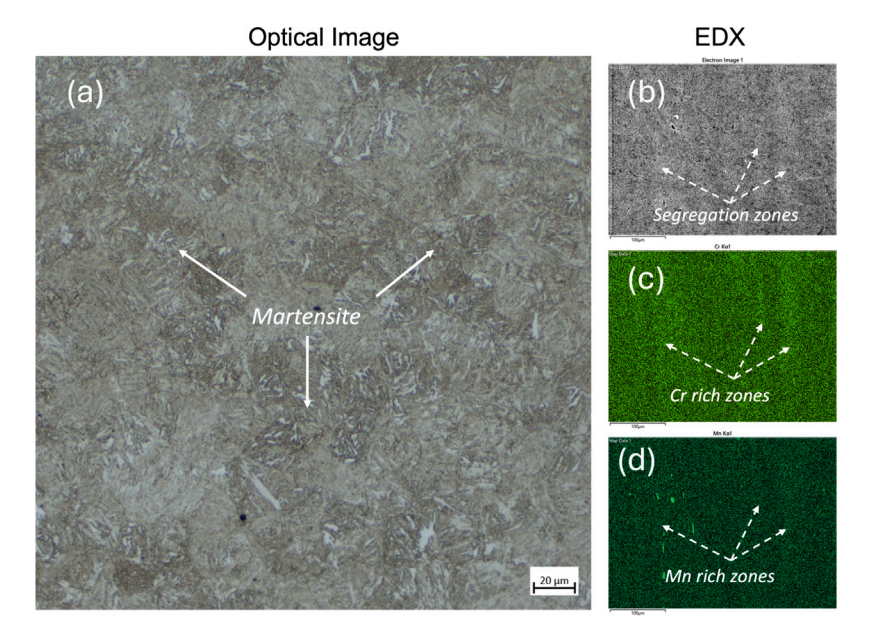
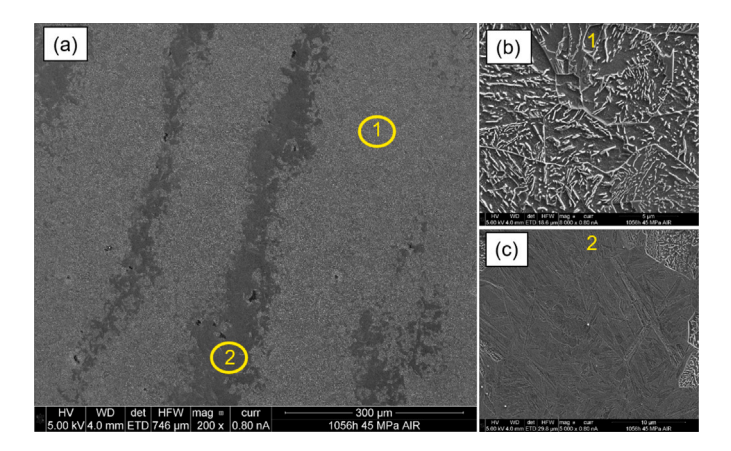


Fig. 3. Detailed microstructural analyses of undeformed material showing (a) Optical image of undeformed 4140 steel depicting a complete martensitic structure and (b), (c) and (d) SEM-EDX maps indicating segregation of Cr and Mn. The segregation patterns show vertical bands in the undeformed material.



**Fig. 4.** The secondary electron image of the sample deformed at 1030 °C showing the region of interest (a) and its constituents (b and c). The microstructure consists of narrow bands similar to those seen in Fig. 3. These are regions of martensite while the rest of the material consists of bainite.

of samples hammer forged at 1030 °C and 1300 °C are shown in Fig. 5(b) and Fig. 5(c) respectively. The average grain size (of the marteniste and bainite packets) of the former is  $\approx \! 10~\mu m$ , the latter possess a larger average grain size of  $\approx \! 40~\mu m$ . The smaller grain size in Fig. 5(b) is caused by slower grain growth at lower forging temperature (1030 °C) and the presence of narrow bands comprising  $\approx \! 12\%$  area fraction within the microstructure. However, for samples forged at 1300 °C, faster grain growth at higher processing temperature and the presence of the narrow bands at lower area fraction ( $\approx \! 6\%$ ) resulted in relatively higher average grain size within the microstructure.

In summary, the resultant microstructure after hammer forging appears to be a mixture of martensite and bainite with the strong dependence on temperature. The forging temperature influences the grain size of the prior austenite leading to difference in the bainite packet size of the final microstructure after cooling. The observed variation in the microstructure after forging at various temperatures are expected to affect the mechanical properties, thereby influencing the performance of the steel. Such heterogeneities in the high-temperature microstructure during forging could be one of the main factors that manifested as variations in deformed shapes in Fig. 1(b). In order to

understand the effect of material and process parameters on the flow of metals (i.e. deformed shapes) during hammer forging, a detailed finite element analysis is employed in the next section.

#### 3. Numerical framework

This section first describes the simulation setup used in the current study. Next, it outlines the constitutive model used to predict the thermomechanical response. Finally, a detailed overview of the calibration process, used to obtain optimal parameters, is presented.

## 3.1. Finite element analysis of hammer forging

Hammer forging simulations were conducted using DEFORM®, a commercial finite element analysis software designed for metal forming operations [32]. The workpiece geometry was defined as a cylinder (outer radius — 32.5 mm, wall thickness — 16.25 mm, height — 20 mm), following the experimental setup (Fig. 6(a)). This workpiece was used across four stages to replicate experiments of Hill et al.:

- 1. Heating up stage
- 2. Transfer from a furnace onto a die (Fig. 6(a))
- 3. Dwell on a die (Fig. 6(b))
- 4. Hammer forging (Fig. 6(c))

Upper and lower dies were introduced depending on the stage. In the first stage, nodes were assigned the initial temperature, assuming a homogeneous temperature distribution. Then, the heat transfer between air and metal was modelled in the second stage. The third stage introduced the bottom die for simulating heat conduction during the dwell, and in the final stage, movement of the top die simulated hammer forging.

Accurate mesh size is crucial for capturing local field fluctuations. In order to obtain the optimum mesh size, a mesh refinement study was performed to analyse strain distribution after forging with a varying number elements. Fig. 7 shows strain distributions for 500, 1000, 1500, and 2000 elements. Minimal changes in strain distribution beyond 1500 elements indicate that this is the optimal element count.

Boundary conditions included friction between the workpiece and dies, and heat transfer between the workpiece and its surroundings. Dry friction at elevated temperatures was modelled using the constant shear

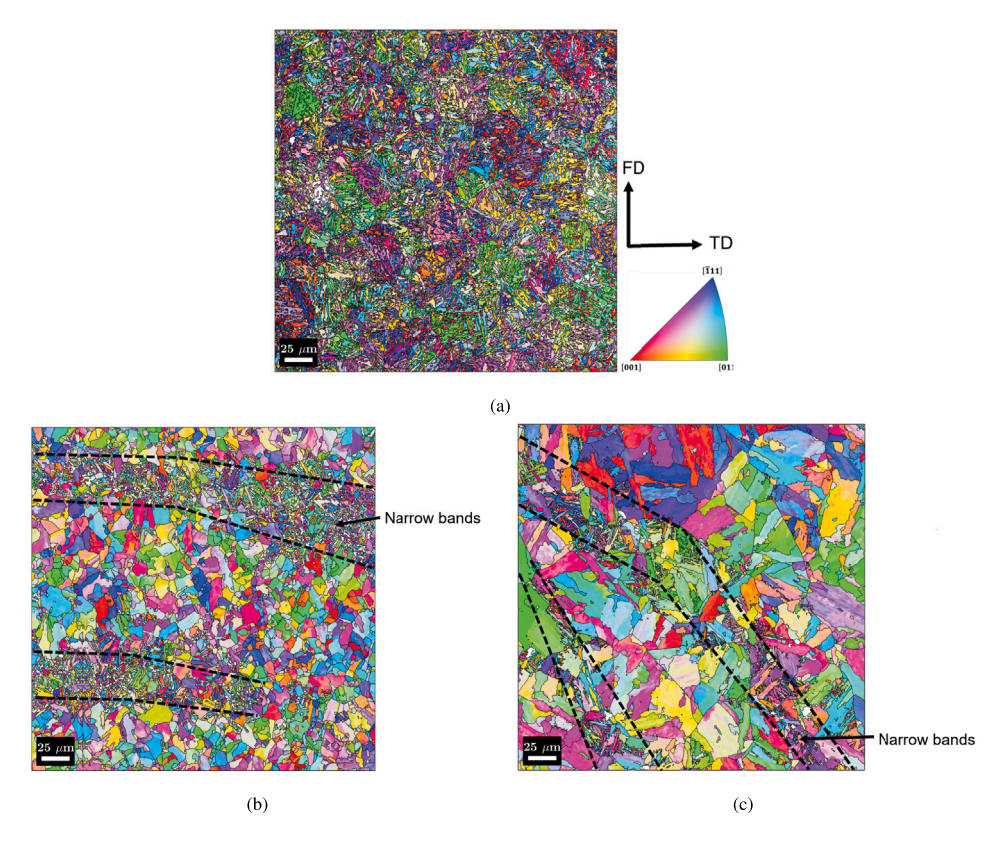


Fig. 5. IPF-Z maps showing indexed-BCC crystal structure from microstructures of (a) undeformed, (b) Hammer forged at 1030 °C and (c) Hammer forged at 1300 °C of 4140 steel. FD refers to the forging direction, while TD the transverse direction. (For interpretation of the references to colour in this figure legend, the reader is referred to the Web version of this article.).

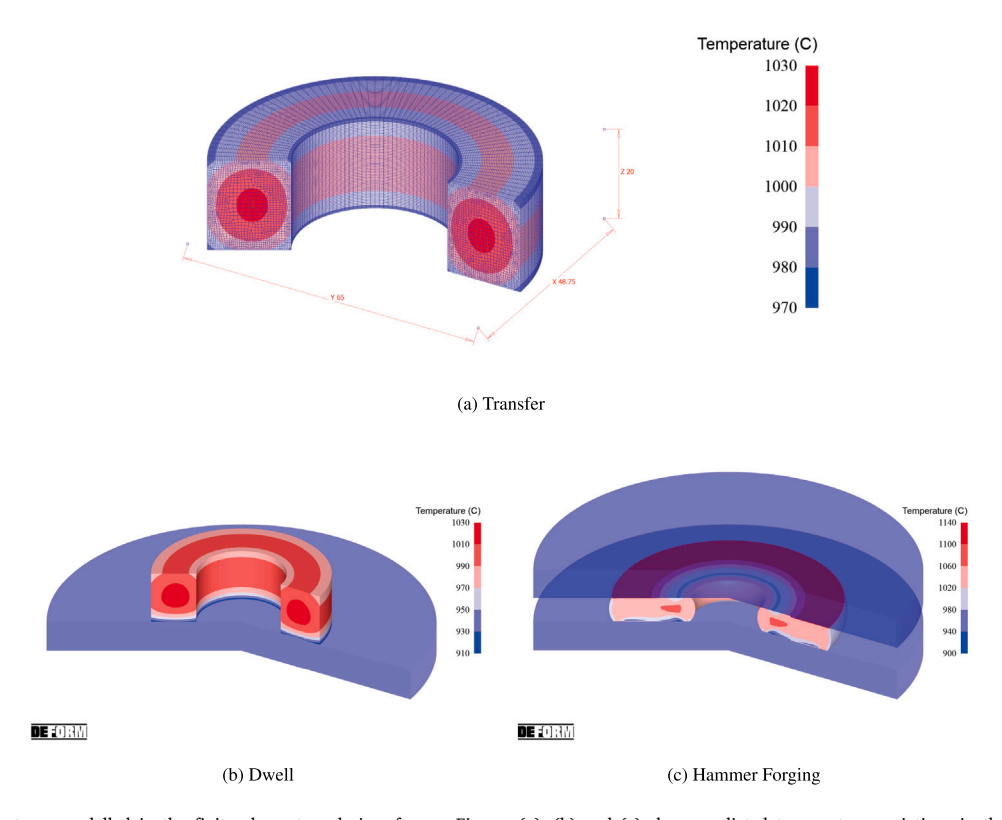


Fig. 6. Hammer forging stages modelled in the finite element analysis software. Figures (a), (b) and (c) show predicted temperature variations in the component at different process stages. Undeformed geometry is displayed on figures (a) and (b).

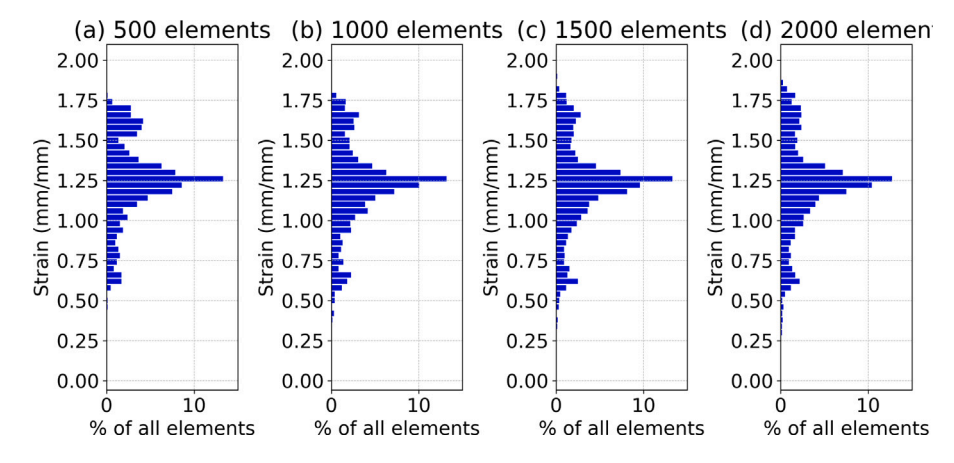


Fig. 7. The change in a distribution of effective strain within a component after forging depending on a number of elements. The strain distribution stabilises in models with more than 1500 elements.

friction law, with a friction factor of 0.7 for forging [32,33]. The heat transfer coefficient between the workpiece and environment was set to 25  $\frac{W}{m^2 \cdot K}$ , while the heat transfer coefficient between the workpiece and both dies was set 500  $\frac{W}{m^2 \cdot K}$  during the dwell stage, increasing to  $5 \cdot 10^3$   $\frac{W}{m^2 \cdot K}$  during hammer forging [32].

Movement controls were applied to both dies: the upper die replicated hammer movement, while the lower die remained stationary. Deformation continued until the hammer's kinetic energy was dissipated by plastic and elastic deformation. The hammer's blow energy was  $21.5 \cdot 10^6 \ N \cdot m$ , and its mass was  $1334 \ kg$ . Blow efficiency ( $\eta$ ) was calibrated against experimental observations.

Each operation required the configuration of simulation controls. The transfer and dwell stages were duration-controlled, wherein 3 s was considered for transfer and 1 s for dwell before forging. An adaptive time step (0.001 to 5 s) was used to improve simulation efficiency, requiring the maximum of 3000 steps for the transfer stage and 1000 steps for the dwell stage. Further, a stroke per step equal to 0.05 mm/step was used for hammer forging simulations.

## 3.2. Constitutive equation for modelling flow stress

To accurately model hammer forging, it is essential to implement a model that includes strain rates beyond the standard experimental range. In the current study, this is achieved by using the hyperbolic sine relationship between stress and strain rate [19], which is widely adopted in industry for simulating steel deformation at elevated temperatures. The equation is

$$\dot{\varepsilon} = A[\sinh(\alpha\sigma)]^n \exp(-Q/(RT)),\tag{1}$$

where Q, n, A,  $\alpha$  are optimised parameters. Q — the activation energy (J/mol), which defines material's softening with increasing temperature. *A* is the parameter that linearly scales the overall magnitude of the strain rate  $\dot{\varepsilon}$ , while  $\alpha$  stretches or condenses the stress  $\sigma$  in the argument of the hyperbolic sine function.  $\alpha$  directly influences how sensitive the material's strain rate is to stress. A higher  $\alpha$  leads to more pronounced sensitivity to stress changes, while a lower  $\alpha$  leads to more gradual changes in the strain rate with stress. n characterises the hardening rate with an increasing strain rate. The physical significance of these parameters is investigated only in a handful of studies [34,35]. While it is reported that the parameters n and  $\alpha$  are constants independent of temperature, composition and microstructure of the material, the activation energy is shown to be a function of alloying elements of steels. In particular, it is demonstrated that *Q* decreases with the carbon content, while it increases with the other alloying elements. It is also suggested that A varies with the activation energy and plays a significant role in determining the peak stress during thermomechanical processing [34,35]. This implies that the parameters A and Q can be

employed to reflect variations in the composition, and therefore the microstructure, of steels, which may have resulted in the differences in deformed geometries in Fig. 1(b)

An alternative form of Eq. (1) exists, where the stress is predicted as the function of  $\dot{\epsilon}$  and T, given as

$$\sigma = (1/\alpha)\sinh^{-1}[(Z/A)^{(1/n)}],\tag{2}$$

where Z is a Zener–Hollomon parameter, which can be calculated by  $Z=\dot{\epsilon}e^{Q/(RT)}$ . It is evident from Eq. (2) that the stress ( $\sigma$ ) is constant, if the relationship between Z and A maintains. Hence, if the model parameters n and  $\alpha$ , as well as the process state variables T,  $\sigma$ , and  $\dot{\epsilon}$ , are constant, both Eqs. (1) and (2) will yield the same outputs as long as  $e^Q/A$  remains constant.

Due to its simplicity, the stated Eq. (1) cannot fully represent material behaviour. Instead, it operates based on the assumption that flow stress remains constant regardless of strain. The model ability can be expanded to account for strain hardening as well as softening due to recrystallisation. However, the latter is excluded in the current study as the specimen undergoes high deformation rates during hammer forging allowing a limited scope for the recrystallisation process during deformation. Therefore, the reduction in the strain hardening rate  $(\partial \sigma/\partial \varepsilon)$  would only result from dynamic recovery of dislocations. As the strain increases, the stress  $\sigma$  approaches  $\sigma^*$ , where there is an equilibrium between dislocation generation and recovery. The flow stress can be modelled as follows [36]:

$$\sigma = [\sigma^{*2} + (\sigma_0^2 - \sigma^{*2})e^{-\beta\epsilon}]^{0.5},\tag{3}$$

where  $\sigma_0$  is the yield,  $\sigma^*$  — the steady-state stress due to dynamic recovery and  $\beta$  is the coefficient of dynamic recovery. When the plastic  $\varepsilon$  equal to 0, Eq. (3) results in the flow stress equal to the yield stress ( $\sigma = \sigma_0$ ). As  $\varepsilon$  increases, the term  $e^{-\beta \varepsilon}$  diminishes to 0, resulting in  $\sigma = \sigma^*$ . Both  $\sigma^*$  and  $\sigma_0$  are predicted by the hyperbolic sine model (Eq. (2)). Therefore, two sets of parameters are derived and used, which are  $\sigma^*$ ,  $Q^*$ ,  $n^*$ ,  $A^*$  and  $\sigma_0$ ,  $Q_0$ ,  $n_0$ ,  $A_0$ .

## 3.3. Derivation of model parameters

For the convenience of parameter calibration, the natural logarithm of Eq. (1) is applied to obtain the linear equation:

$$\ln(\sinh(\alpha\sigma)) = \ln \dot{\varepsilon}/n + Q/(nRT) - \ln A/n \tag{4}$$

This equation defines the linear relationship between modified process state variables  $\ln(\dot{\varepsilon})$ ,  $\ln(\sinh(\alpha\sigma))$  and  $T^{-1}$ . The first parameter to obtain is n. It is derived by differentiation of  $\ln(\sinh(\alpha\sigma))$  over  $\ln \dot{\varepsilon}$ , which gives:

$$n = \left[\frac{\partial \ln(\sinh(\alpha\sigma))}{\partial \ln \dot{\epsilon}}\right]^{-1} \tag{5}$$

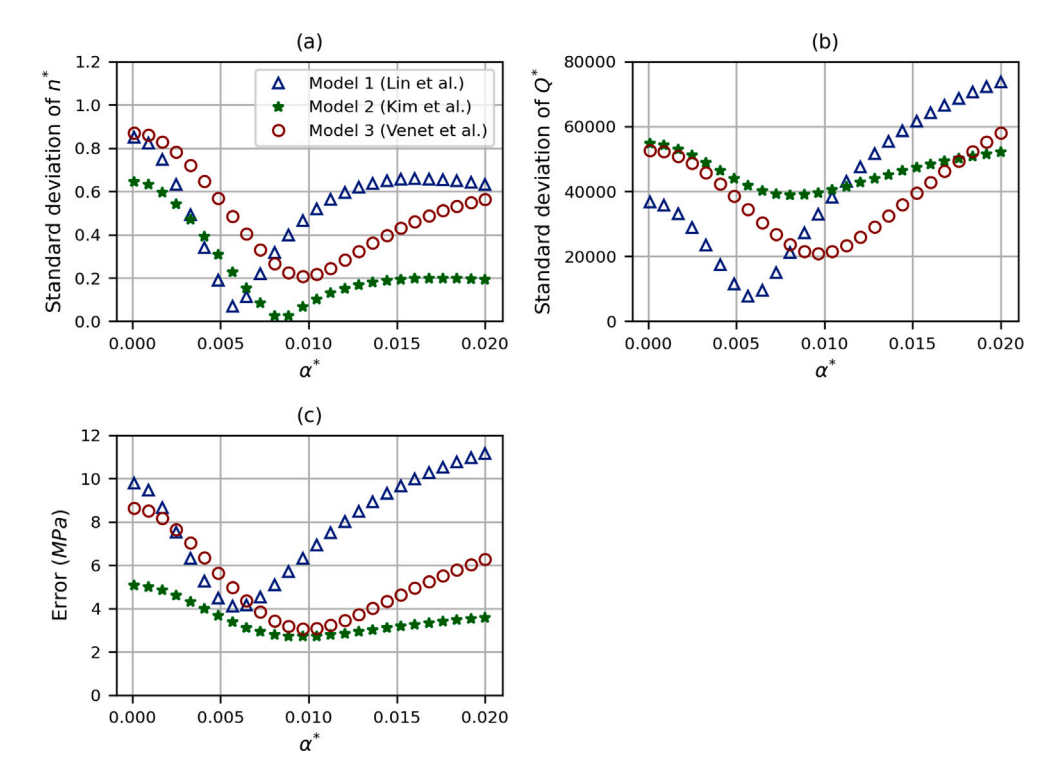


Fig. 8. The change of modelling output while varying  $\alpha^*$ : (a) Standard deviation of  $n^*$ ; (b) Standard deviation of  $Q^*$ ; (c) Root mean squared error of predictions. The model performs optimally at  $\alpha^*$  within the range of 0.005 to 0.01.

Then, Q is obtained from the derivative of  $\ln(\sinh(\alpha\sigma))$  over  $T^{-1}$  resulting in

$$Q = \left[\frac{\partial \ln(\sinh(\alpha\sigma))}{\partial(1/T)}\right] nR,\tag{6}$$

where n is the mean of the whole dataset. A is calculated by determining the value of  $\ln(\sinh(\alpha\sigma))$  at  $\ln\dot{\epsilon}=0$  through a regression analysis. The parameter is calculated as follows:

$$A = (\sinh[\alpha\sigma(\dot{\varepsilon} = 1)])^n \cdot e^{-\frac{Q}{RT}}$$
(7)

This way A is determined for each temperature condition. The parameter  $\alpha$  significantly impacts n, Q, and A. Determining  $\alpha$  involves testing various  $\alpha$  values while fitting the other parameters. For each  $\alpha$ , the model's performance is assessed by predicting stress ( $\sigma$ ) using Eq. (2) and the fitted parameters. The optimal  $\alpha$  is then chosen as the one that minimises the error between predicted and experimental stress values.

The dynamic recovery coefficient is obtained by applying the natural logarithm to Eq. (3), resulting in the transformed equation:

$$\ln(\sigma^{*2} - \sigma) = \ln(\sigma^{*2} - \sigma_0^2) - \beta \varepsilon \tag{8}$$

This equation is then fitted to experimental data to determine  $\beta$  under various deformation conditions.

In order to calibrate the constitutive model, the experimental thermomechanical responses recorded by Lin et al. [19], Kim et al. [18] and Venet et al. [20] under varying elevated temperatures and strain rates are considered. These studies collectively offer a comprehensive independent dataset essential for reliable model calibration.

## 4. Results and discussion

This section first describes the calibration results of the constitutive model and discusses the effect of uncertainties within these parameters on hammer forging. Then, the role of hammer forging parameters in the post-forging geometry predictions is discussed in detail.

#### 4.1. Constitutive model

#### 4.1.1. Model parameters to predict $\sigma^*$

The initial model parameters are derived to first predict the peak stress ( $\sigma^*$ ). The standard deviation in  $n^*$  and  $Q^*$ , and the error in stress predictions are shown in Fig. 8(a), (b) and (c) respectively. The model demonstrates the optimal performance when  $\alpha^*$  falls within the range of 0.005 to 0.01 MPa<sup>-1</sup>, as illustrated in Fig. 8. In this range, the fitted constitutive model minimises the root mean squared error between predicted and measured  $\sigma^*$ , with the calibrated model showing an error less than 7 MPa (Fig. 8(c)). Furthermore, the standard deviation of both parameters  $Q^*$  and  $n^*$  reaches minimum within the same range of  $\alpha^*$  (Figs. 8(a) and 8(b)), indicating reduced dependency on process inputs. Therefore, the model would be robust and reliable, independent of variations in the input data. The central value within the observed optimal range for  $\alpha^*$ , which is 0.0075 MPa<sup>-1</sup>, is selected for subsequent calibrations. It is worth noting that the obtained range (0.005 to 0.01  $MPa^{-1}$ ) and the average values of  $\alpha^*$  are in line with other numerical studies (e.g. [37]).

Based on three datasets containing flow stress data and the optimal value of  $\alpha^*$ , three separate sets of model parameters are derived as shown in Table 2. These parameters represent the mean values of the corresponding distributions of parameters obtained after calibration. Figs. 9(a) and 9(b) show the relationship between the optimised parameters of the constitutive model, which are used to predict the peak stress,  $\sigma^*$ . Generally,  $Q^*$  and  $A^*$  can be considered in combination as there is a strong correlation between these parameters, as illustrated in Fig. 9(a). By using the average value of 5.89 for  $n^*$  from all three datasets, the following relationship between  $Q^*$  and  $\ln(A^*)$  can be derived:

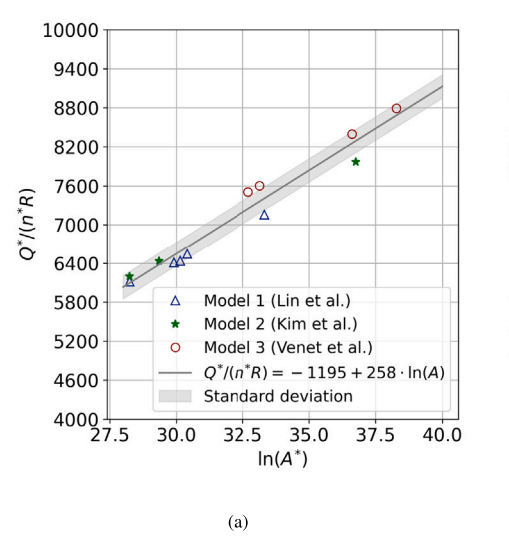
$$Q^* = -58490 + 12628 \cdot \ln(A^*) \tag{9}$$

with a standard deviation of error equal to 8769 J/mol.

The relationship between  $Q^*$  against  $n^*$ , shown in Fig. 9(b), reveals no strong correlation.  $Q^*$  ranges from 307 kJ/mol and 415 kJ/mol, while  $n^*$  is between 5.2 and 6.4 (Fig. 9(b)). The scatter plot indicates

Table 2
Three sets of constitutive model parameters obtained from the flow stress data provided by the specified authors

	$\alpha^*$ (MPa <sup>-1</sup> )	$Q^*$ (J/mol)	n*	$A^*$ (s <sup>-1</sup> )	$\alpha_0 \text{ (MPa}^{-1}\text{)}$	$Q_0$ (J/mol)	$n_0$	$A_0  ext{ (s}^{-1})$
Model 1 (Lin et al.)	0.0075	329 075	6.06	$2 \cdot 10^{13}$	0.0075	240 489	7.03	$1.25 \cdot 10^{11}$
Model 2 (Kim et al.)	0.0075	340 808	5.97	$4.5 \cdot 10^{13}$	0.0075	273 783	7.95	$6.3 \cdot 10^{13}$
Model 3 (Venet et al.)	0.0075	381 174	5.68	$1.9 \cdot 10^{15}$	0.0075	604 778	10.30	$4.2 \cdot 10^{26}$



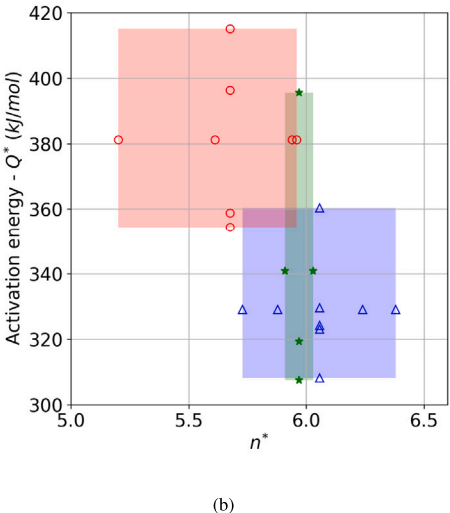


Fig. 9. Relationship between derived model parameters: (a) Linear relationship between  $Q^*/(n^*R)$  and  $\ln(A^*)$ ; (b) The scatter plot of  $Q^*$  against  $n^*$  with corresponding bounding boxes covering each dataset used for calibration.

that the alloy in Lin et al. and Kim et al. [18,19] showed approximately close response to a change in deformation rates and temperatures. This is evident from bounding boxes of these two generated sets of model parameters overlapping each other (Fig. 9(b)). On the other hand, the set of parameters, generated based on the dataset of Venet et al. [20], is on the other spectrum. The material displayed higher activation energy —  $Q^*$ , but lower  $n^*$ . A higher  $Q^*$  indicates that the material in the work of Venet et al. is more sensitive to temperature changes according to Eq. (6). Averaging constitutive model parameters, used to predict maximum stress, gives values of  $Q^*$ ,  $n^*$ , and  $A^*$  as 350352 J/mol, 5.9, and  $1.2 \cdot 10^{14}$  s<sup>-1</sup>, respectively. Note that the arithmetic mean was used for  $Q^*$  and  $n^*$ , while the average for  $A^*$  was calculated logarithmically, given Eq. (4).

## 4.1.2. Model parameters to predict $\sigma_0$

The published flow stress data also provided yield stress values  $(\sigma_0)$  at different temperatures (T) and strain rates  $(\varepsilon)$ , which are used to obtain  $Q_0$ ,  $n_0$  and  $A_0$ . In order to ensure comparability between two sets of model parameters for predicting both  $\sigma_0$  and  $\sigma^*$ ,  $\alpha_0$  is set equal to  $\alpha^*$  as  $\alpha$  significantly influences the other model parameters. Table 2 outlines the derived parameters to predict  $\sigma_0$ . In two sets of parameters (Model 1 and 2), the activation energy  $Q_0$  is significantly less than  $Q^*$ , indicating that the yield stress is relatively less dependent on temperature changes in comparison to peak stress  $(\sigma^*)$ . On the contrary, Model 3 predicts the material yield stress to be more sensitive to temperature variations, characterised by significant  $Q_0$ , which is bigger than corresponding  $Q^*$ . Given the set of calibrated  $Q_0$  and  $\ln(A_0)$ , the relationship between both parameters was derived:

$$Q_0 = -28300 + 10263 \cdot \ln(A_0) \tag{10}$$

## 4.1.3. Dynamic recovery coefficient

The calibration results of the dynamic recovery coefficient,  $\beta$ , for different process conditions are presented in Fig. 10.  $\beta$  is observed to be higher at lower strain rates, specifically those below 1 s<sup>-1</sup>. The effect of

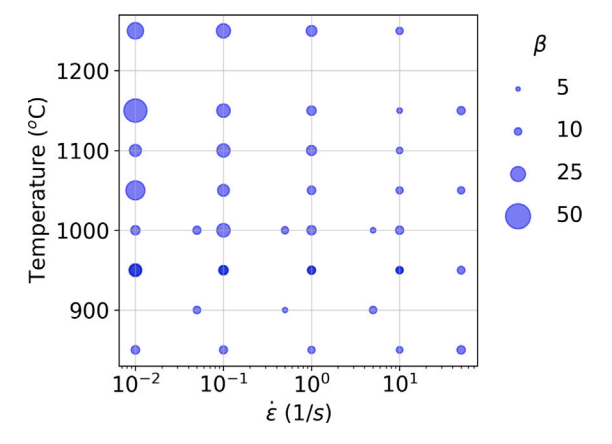


**Fig. 10.** The dependency of the dynamic recovery coefficient ( $\beta$ ) on process conditions.  $\beta$  shows greater sensitivity to temperature at lower strain rates, and increases as temperature rises.

temperature on  $\beta$  is only evident at these lower strain rates, indicating that  $\beta$  increases as temperature rises. In contrast,  $\beta$  at higher strain rates remains minimal, regardless of temperature. These observations indicate that the dynamic recovery coefficient is a function of a strain rate and temperature as noted in other studies (e.g. [38]). Further, the trends in  $\beta$  reported in the current study are comparable with other numerical and experimental observations (e.g. [39,40]), which demonstrated that dynamic recovery is highest at higher temperatures and lower strain rates. In addition, from Fig. 10, for the strain rates of 10 and 50 s<sup>-1</sup>, the average  $\beta$  coefficient is 9.5 with the standard deviation of 1.61. Due to the lack of compression stress–strain data at strain rates above 50 s<sup>-1</sup>, a  $\beta$  value of 9.5 is used to predict the flow stress at higher strain rates.

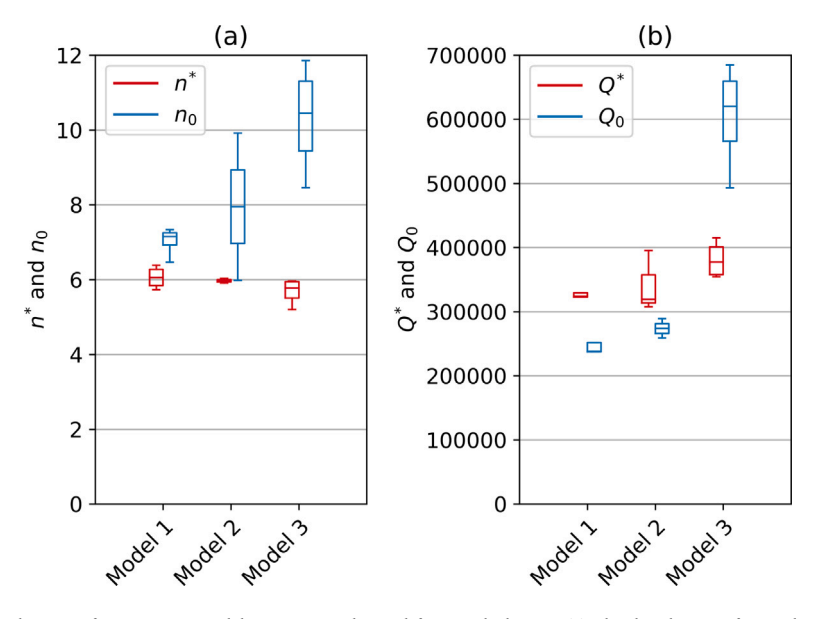


Fig. 11. Boxplots illustrating the distributions of constitutive model parameters obtained from each dataset: (a) The distribution of  $n^*$  and  $n_0$ ; (b) The distribution of  $Q^*$  and  $Q_0$ . Constitutive model parameters used to predict the yield stress ( $n_0$  and  $Q_0$ ) exhibit a greater variation.

#### 4.1.4. Uncertainty in flow stress

The heterogeneity in material response can be effectively addressed by using a range of model parameters within the hyperbolic sine model, instead of relying only on mean values. This approach allows for generation of a wider range of stress–strain  $(\sigma - \varepsilon)$  relationships, thus accommodating the heterogeneity observed in materials. Achieving this involves sampling parameters from their respective distributions and integrating them into stress prediction. The distributions of parameters is shown in Fig. 11. The figure shows considerable variations in  $n_0$  and  $Q_0$  compared to that of  $n^*$  and  $Q^*$ . This resulted in the variation of  $\sigma^*$  across the three models more closely aligned compared to that of predicted  $\sigma_0$ . Due to the large span in  $Q_0$  and  $n_0$ , the associated uncertainty was quantified by sampling parameters from three distinct distributions separately. Then, the predictions of corresponding stress values are made, followed by the combination of these predictions through the calculation of average values.

Fig. 12(a) shows the measured uncertainties in prediction of the peak stress  $(\sigma^*)$ , obtained by sampling and propagating model parameter values from their corresponding distributions. These uncertainties represent the sigma confidence interval of predictions (an example shown in Fig. 12(b)). From the figure, the model shows that confidence in predictions increases as temperature rises. At lower temperatures, the strain rate has a little effect on prediction confidence. However, at higher temperatures, increased strain rates significantly reduce confidence. This behaviour can be attributed to the Arrhenius equation exp(Q/(RT)) in the constitutive model, whereby increasing temperature mitigates the effect of the activation energy (Q). As a result, there is a greater amplification effect of  $\dot{\varepsilon}$  on stress variations in the Zener–Hollomon parameter —  $Z = \dot{\varepsilon} exp(Q/(RT))$ .

## 4.2. Hammer forging modelling

As mentioned earlier, hammer forging parameters include initial temperature of a billet, transfer time from an induction heater onto a lower die, dwell time (the time before the onset of hammer forging), temperatures of top and bottom dies, friction between a billet and dies and the blow efficiency  $(\eta)$ . The calibration of model parameters and the effect of uncertainties are discussed thus far. In the following subsections, the calibrated model parameters are first used to obtain the optimal blow efficiency. Then, model parameters and blow efficiency are validated against experimental observations. Finally, the effect of uncertainties in model parameters on the post-forging specimen geometry is presented in detail.

#### 4.2.1. Hammer blow efficiency

One of crucial process parameters is the blow efficiency. The model parameters established in the previous section can be used to estimate the hammer blow efficiency  $(\eta)$ . Fig. 13 shows the variation in predicted height after forging, using the three sets of model parameters (Table 2), with respect to corresponding blow efficiencies. The grey area in the figure indicates the variation in experimental measurements reported in Hill et al. [26]. The figure shows negligible differences in the predicted post-forging height for the three sets, as observed in simulations at 1030 °C (Fig. 13(a)) and 1300 °C (Fig. 13(b)). This is due to the negligible difference in the mean derived n across the three sets of model parameters, while ln(A) scales linearly with the mean activation energy Q, and therefore compensates a corresponding change in Q. The efficiency of hammer forging at 1030 °C is predicted to be 50%. At this level, the finite element analysis predicts the height of the deformed specimen to be 9.61 mm, which is close to the measured height of 9.5±0.2 mm [26]. Further, increasing temperature from 1030 °C to 1300 °C in simulations results in lower efficiency estimates, where accurate predictions of the post-forging height, compared to the experimental results (7.6±1 mm [26]), are achieved at  $\eta = 40\%$ . These predicted blow efficiencies are in good agreement with other studies [28,29]. In addition, the small difference between blow efficiency estimates at 1030 °C and 1300 °C indicates that the derived constitutive models accurately predict the softening of material as temperature increases.

#### 4.2.2. Validation of the numerical hammer forging analyses

The performance of the deformation predictions within the work-piece after hammer forging is now validated against the experimental observations. It is observed earlier in Section 2.2 that the samples before deformation are characterised by vertical and straight segregation bands, which are parallel to the forging direction. These bands may show distinct distributions after deformation, which are potentially driven by local accumulation of strain within the deformed samples. Therefore, these distributions in experimental observations are compared with that of predicted effective strain to validate the constitutive model and hammer forging simulations.

The predicted effective strain distributions and the segregation bands observed in experiments within the workpiece forged at 1030 °C are shown in Fig. 14. The prediction was made using  $\sigma$  -  $\varepsilon$  curves generated by the constitutive model (Section 3.2) and the associated parameters  $Q^*=350352$  J/mol,  $n^*=5.9$ ,  $A^*=1.2\cdot 10^{14}$  s<sup>-1</sup>,  $Q_0=373016$  J/mol,  $n_0=8.4$ ,  $A_0=1.5\cdot 10^{17}$  s<sup>-1</sup>, which are averages across

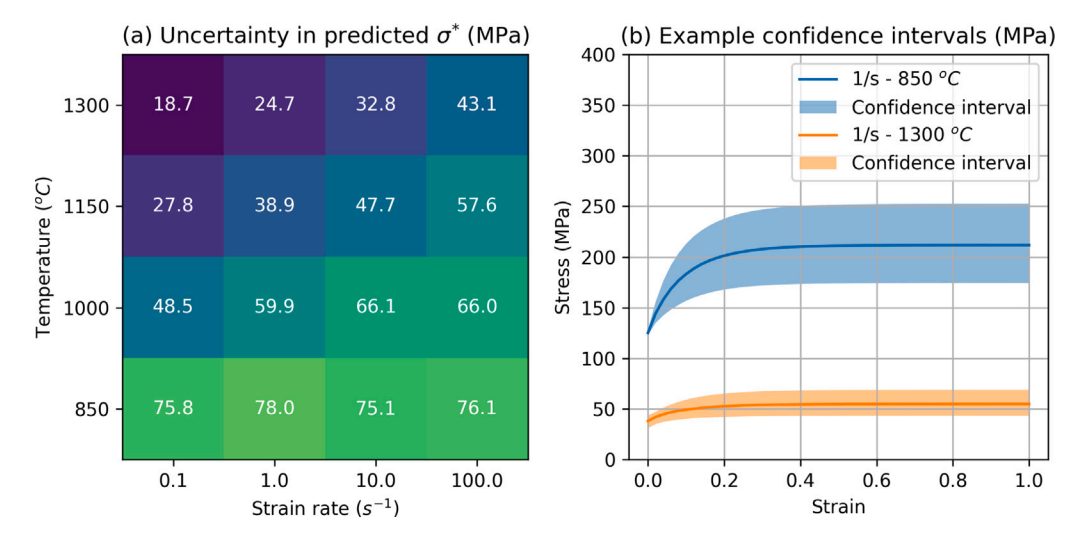


Fig. 12. Uncertainty in  $\sigma^*$  predictions: (a) The change in uncertainty with the temperature and strain rate. The constitutive model is more confident at elevated temperatures and reduced strain rates. (b) Examples of confidence intervals at different temperatures, given a strain rate of 1 s<sup>-1</sup>.

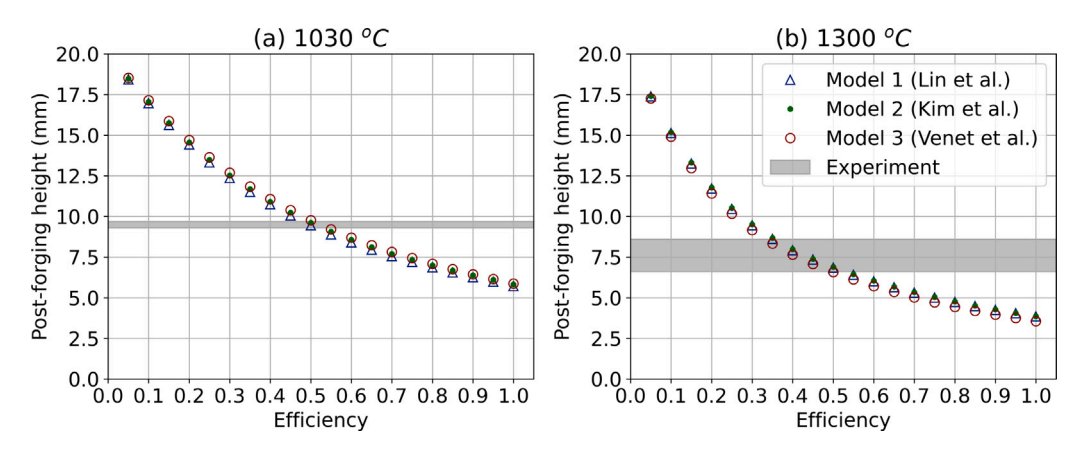


Fig. 13. The influence of blow efficiency on the final component height after deformation in simulations using three calibrated constitutive models. Figures (a) and (b) shows the optimal efficiency values at two testing temperatures, 1030 °C and 1300 °C respectively, at which the predicted height falls within the range of experimental measurements.

3 datasets presented in Table 2. The model was configured with blow efficiency of 50%, while transfer and dwell time were set to 3 s and 1 s respectively. There is a close match between the predicted strain patterns and observed segregation patterns (deformation flow lines). The finite element model predicts the flow lines, slightly off-centre to the left, which exhibit bending in both directions corresponding to regions of high strain. Similar locations and flow patterns are observed in the experimental workpiece after deformation, further confirming the reliability of the model. In addition, this also confirms that the segregation bands within materials can be employed as indicators of strain distribution after deformation. Further, the friction at the die-workpiece contact dictates the final shape of a component after forging. The predicted cross-sectional shape shown in Fig. 14 matches closely with the shape observed in the experiment, which validates the boundary conditions applied in simulations. Here, the outer boundary appears to possess less curvature as the outer region of the workpiece experiences more sliding compared to that of the inner region.

# 4.2.3. Propagation of uncertainty in stress predictions to post-forging geometry

The stress response of a material reflects its local microstructure and boundary conditions. The variations in this response, due to inherent heterogeneity, can be captured by introducing uncertainties in constitutive model parameters, resulting in a distribution of stress–strain outcomes. One approach is to randomly sample parameters  $(Q^*,$ 

 $Q_0$ ,  $n^*$ , and  $n_0$ ) from distributions (Fig. 11) and use them to generate stress–strain relationships for finite element simulations, which is computationally expensive. Alternatively, parameters can be sampled and applied in the hyperbolic sine model to predict stress distributions across temperature and strain rates. The confidence intervals  $(\pm \sigma_{std}, \pm 2\sigma_{std})$  from these distributions provide bounds for predicted stress. Applying these bounds in finite element models captures the range of material flow responses.

The distributions of predicted post-forging heights for the selected confidence interval ( $\pm 2\sigma_{std}$ ) at different temperatures and blow efficiency of 40% are shown in Fig. 15, along with the measured post-forging heights at 1030 °C and 1300 °C. The model showed the greater variation in predicted geometry compared to the observed measurements at both temperatures, due to the chosen confidence intervals. Notably, uncertainties in height predictions to some extent overlap with the observed variations in geometry at both temperature conditions. The hammer forging model predicts the component height with corresponding uncertainties of  $10.62\pm1.46$  mm and  $7.76\pm1.54$  mm, while the experimental observations are  $9.5\pm0.2$  mm and  $7.6\pm1$  mm at 1030 °C and 1300 °C, respectively.

## 4.3. Parametric studies

A multifactorial design of experiments (DoE), summarised in Table 3, with 3,600 simulations, investigates how process parameters affect post-forging geometry and examines how initial uncertainties

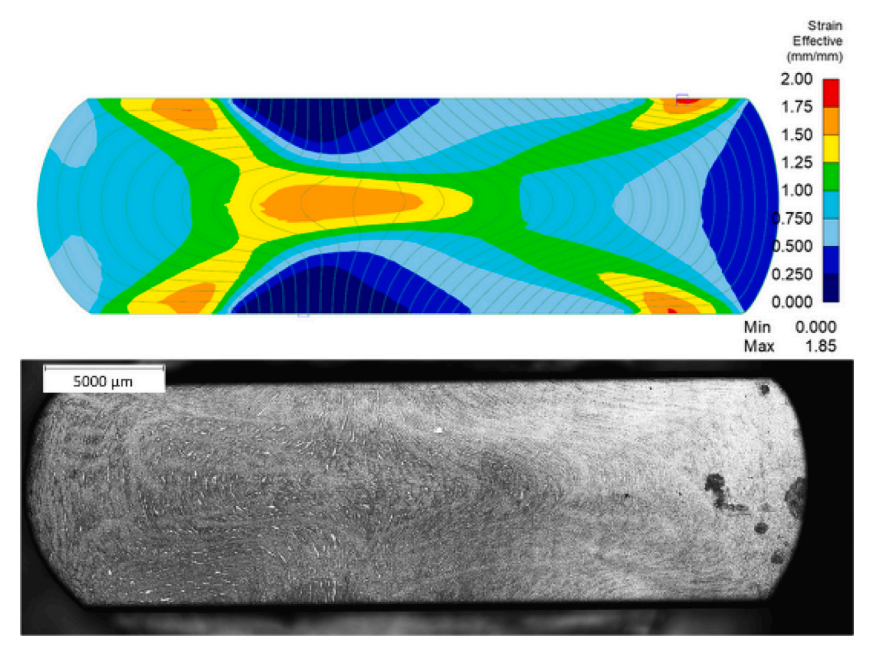
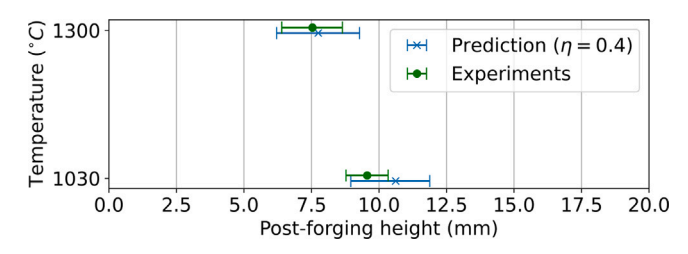


Fig. 14. The comparison between the predicted material flow lines (effective strain distributions) and the segregation bands observed in the cross-section of a sample hammer forged at 1030 °C. Both the predicted lines and observed bands show a close match. Note that the experimental bands are vertical in nature before deformation as shown in Fig. 3.



**Fig. 15.** Predicted uncertainty in post-forging height at a blow efficiency of 40%, varying with temperature, compared to observed variability in component height from forging experiments.

Table 3
List of parameters in the parametric studies.

List of parameters	Values		
Initial temperature (T)	895 °C, 1030 °C, 1165 °C, 1300 °C		
Blow efficiency $(\eta)$	20%, 40%, 60%, 80%, 100%		
Friction coefficient (m)	0.3, 0.6, 0.7, 0.8		
Transfer time $(t_1)$	1 s, 3 s, 9 s		
Dwell time $(t_2)$	1 s, 3 s, 9 s		
Flow stress	$-2\sigma_{std}$ , $-\sigma_{std}$ , Mean, $+\sigma_{std}$ , $+2\sigma_{std}$		

in flow stress predictions impact geometry prediction uncertainties under varying process conditions. The DoE included  $\pm \sigma_{std}$  and  $\pm 2\sigma_{std}$  confidence intervals derived from the corresponding distributions of stress predictions.  $-2\sigma_{std}$  in Table 3 represents the application of the softest alloy in the finite element analysis, while the confidence limit at  $+2\sigma_{std}$  corresponds to the hardest alloy within the predicted range of alloy responses. That is, this accounts for potential variations in chemical compositions and starting microstructures (driven by processing history) of the material.

## 4.3.1. Correlation between process parameters and modelling outputs

The relationship between modelling inputs and outputs was examined using Spearman rank correlation analysis, as shown in Fig. 16. In the correlation matrix, coefficients closer to -1 or 1 indicate stronger relationships. The analysis identified blow efficiency as the most dominant factor, impacting all deformation-related outputs such as mean

strain, strain rate, maximum outer radius, and post-deformation height. The initial temperature was the second most significant factor. Flow stress variations also influenced deformation but they were less impactful than other parameters. In addition, transfer and dwell times had limited effects, with dwell time influencing lower die temperature but not significantly affecting friction at the die-component interface and final geometry. The changes in friction coefficient showed no correlation with outputs. The observed weak correlation between the stated process parameters (transfer time, dwell time and friction coefficient) and modelling predictions is likely due to a variability introduced by other inputs, which can be verified by performing controlled experiments.

## 4.3.2. Effect of time intervals

Steel manufacturing frequently faces disruptions that affect material properties and final shapes of components. The delays between stages, such as transfer and dwell times before forging, are important factors for engineers to evaluate. Figs. 17(a) and 17(b) display the effect of these process parameters on the specimen's final height at different temperatures. The figures show that the dwell time has more pronounced effect on the final shape compared to that of the transfer time. Here, higher dwell times required a larger increase in the initial temperature in order to maintain consistent geometry.

#### 4.3.3. Effect of friction

Friction is known to significantly influence the final shape and properties of a forged component. In this study, a friction coefficient of 0.7 is used to represent dry hot forging conditions (see Section 3.1). In addition, in order to study the effect of friction further, an additional friction coefficient of 0.3 is also considered [32], representing a lubricated hot forging condition. Blow efficiencies of 20%, 60% and 100% are also considered to study their influence in conjunction with friction. Fig. 18 shows the variation in post-forging height for two friction and three blow efficiencies. The figure shows that the role of friction in hammer forging becomes more pronounced with a greater energy input (higher blow efficiency), where a substantial reduction in the height is observed after forging. At higher energy levels, increased friction generates opposing forces that limit component deformation. Frictional impact is more pronounced at higher blow efficiencies due to the larger contact area between the dies and the component, which further amplifies opposing forces, especially with a higher friction

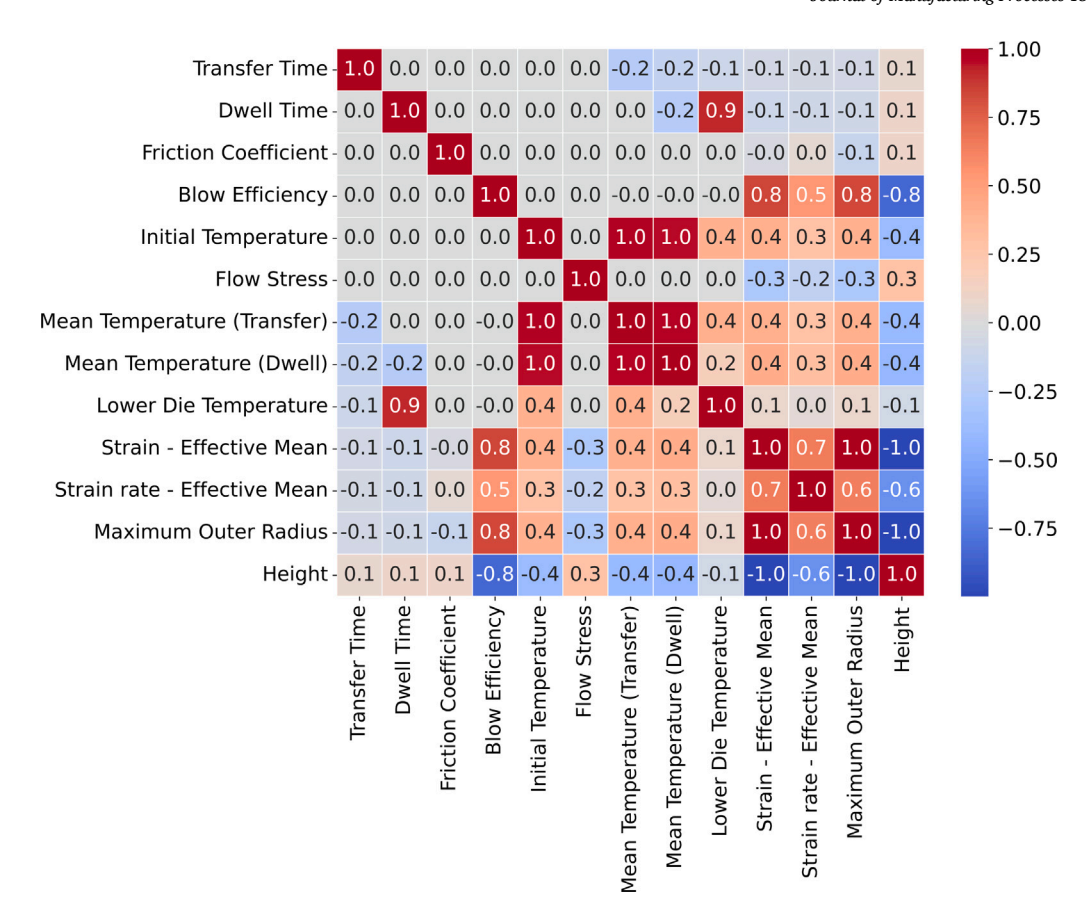


Fig. 16. Spearman Rank Correlation Analysis: This figure shows the relationships between process parameters and modelling outputs. Blow efficiency and initial temperature are the most influential parameters affecting deformation outputs. Flow stress variations impact final geometry, but transfer and dwell time have minimal effects.

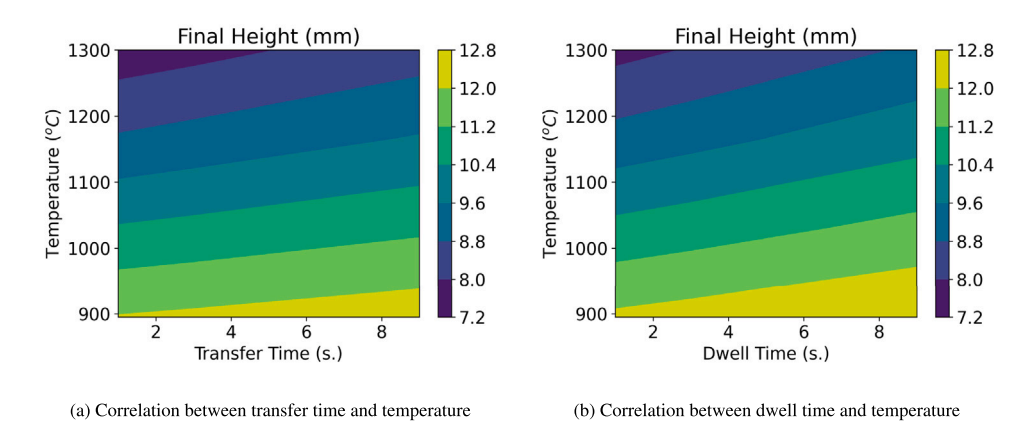


Fig. 17. Correlation between process times and the height after forging at 40% efficiency. The data indicates that dwell time has a more significant impact on height. To maintain consistent geometry, an increase in dwell time should be balanced by a larger increase in the initial temperature.

coefficient. Thus, in addition to reinforcing the need to quantify the blow efficiency of a machine, this analysis also suggests that the friction coefficient should be chosen carefully while simulating hammer forging of components forged using machines with higher blow efficiencies.

## 4.3.4. Uncertainty quantification

As noted earlier, the use of upper and lower confidence limits of the flow stress prediction enables propagation of corresponding uncertainties to the geometry predictions post hammer forging. Fig. 19(a) presents the calculated uncertainties in height and outer radius, predicted at various temperatures and blow efficiencies. These uncertainties are measured by the length of the confidence interval around predictions. The finite element model exhibited decreased confidence in predicting the final height of the component at lower efficiency inputs and elevated temperature. This finding contrasts with the observed uncertainty in flow stress predictions, where the hyperbolic sine model displayed more confidence as temperature increased (Fig. 12(a)). The reason for this difference is that a component is constrained by two

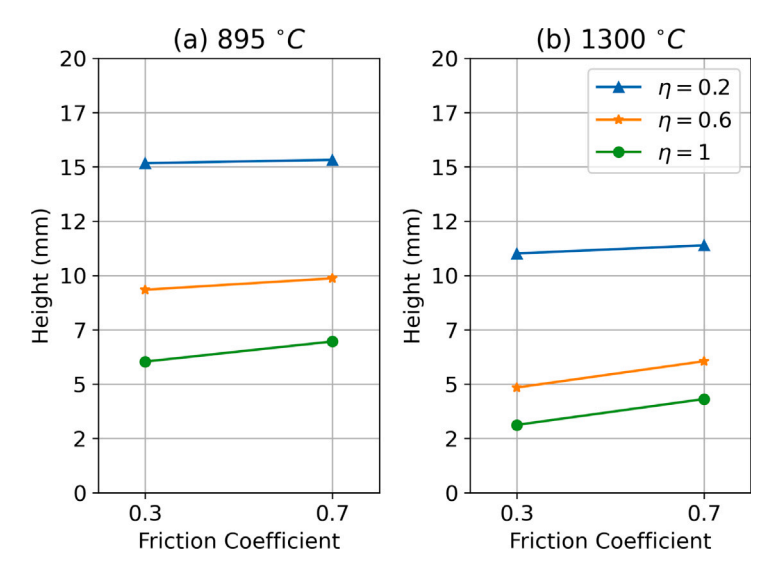


Fig. 18. The effect of friction on the component's height after deformation at low/high temperature, considering the blow efficiency. Friction becomes more significant at higher efficiency.

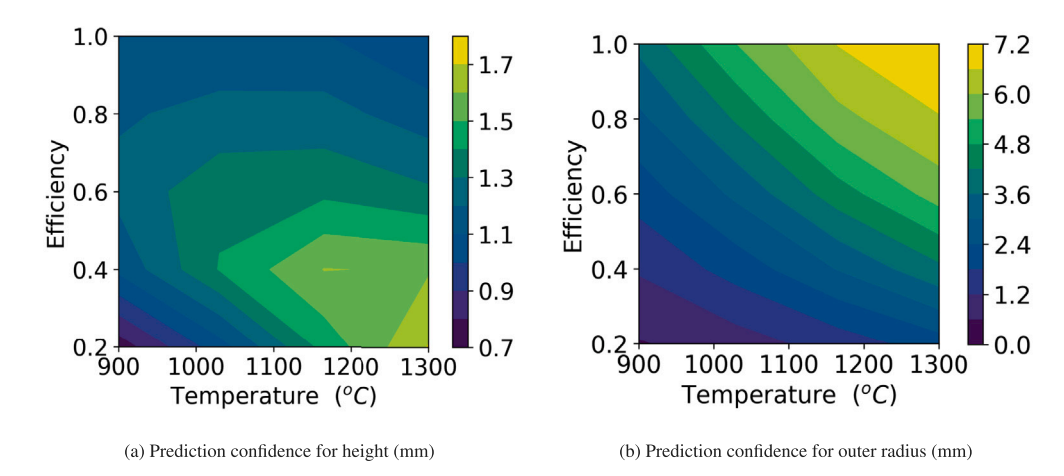


Fig. 19. The effect of blow efficiency and temperature on the uncertainty of predicted component geometry after deformation. Uncertainty in height predictions rises at lower efficiencies and higher temperatures, while uncertainty in outer radius predictions positively correlates with both temperature and blow efficiency.

dies during hammer forging. When blow efficiency is low, the specimen undergoes minimal deformation, causing little change to its top and bottom contact surfaces from their undeformed state. This means that any variations in flow stress will significantly affect the height differences after forging as there are fewer opposing forces exerted by the contact surfaces. In contrast, higher blow efficiency results in greater deformation of the component, leading to larger contact surfaces. Consequently, more hammer force is required during forging to continue the deformation process. Due to the increased hammer force, the height differences after forging become less sensitive to variations in flow stress. This is because the larger contact surfaces create stronger opposing forces that counteract the impact of flow stress variations. This behaviour is also evident when examining Figs. 13a and 13b, which display the greatest reduction of a height at lower efficiency values or energy input, while at higher efficiency there is less reduction in a post-forging height.

## 5. Conclusions

The study optimised the constitutive model based on the hyperbolic sine equation (consisting of  $\alpha$ , Q, n, and A as key parameters) to predict the deformation behaviour of 708M40 steel at elevated temperatures. This optimisation, using published datasets from compression

tests, allowed accurate predictions of steel deformation under specific processing conditions, with corresponding confidence intervals. These predictions were further integrated into finite element analysis of hammer forging, enabling the propagation of uncertainty in flow stress predictions to assess its impact on post-forging geometry.

The key conclusions are as follows:

- 1. The constitutive model was calibrated to 0.0075 MPa<sup>-1</sup> by varying  $\alpha$  to maximise the accuracy of peak stress predictions. In order to achieve consistent model performance, strong correlations between  $Q^*$  and  $A^*$  must be maintained for peak stress predictions, and between  $Q_0$  and  $A_0$  for yield stress predictions. For predicting maximum stress, the parameters  $Q^*$ ,  $n^*$ , and  $A^*$  were optimised to be 350352 J/mol, 5.9, and  $1.2 \cdot 10^{14}$  s<sup>-1</sup>, respectively, based on the average of three model parameter sets.
- 2. Confidence in flow stress predictions increases as temperature rises. However, it decreases at higher strain rates, especially at elevated temperatures. This indicates that the constitutive model becomes less reliable at lower temperatures. The trend is attributed to the exponential term in the hyperbolic sine equation, where higher temperatures reduce the impact of activation energy variability on stress predictions.
- 3. Blow efficiency, calibrated to 50% at 1030 °C and 40% at 1300 °C, enabled accurate height predictions. At 40% efficiency,

the model predicted final heights of  $10.62\pm1.46$  mm and  $7.76\pm1.54$  mm, compared to experimental values of  $9.5\pm0.2$  mm and  $7.6\pm1$  mm at 1030 °C and 1300 °C, respectively. Large uncertainties in height predictions result from the chosen confidence interval  $(\pm2\sigma_{std})$ . Predicted flow lines matched experimental observations, confirming the model's accuracy in simulating deformation.

4. In contrast to the uncertainty trends in flow stress predictions, simulations of hammer forging at higher temperatures showed lower confidence in height predictions, particularly at low blow efficiencies. However, increasing efficiency improves confidence. Higher blow efficiency causes greater workpiece reduction and greater die-metal contact, enhancing resistance to deformation and minimising the effect of flow stress uncertainty.

## CRediT authorship contribution statement

Oleksii Koval: Writing – review & editing, Writing – original draft, Visualization, Validation, Software, Methodology, Investigation, Formal analysis, Data curation, Conceptualization. Anindya Das: Writing – review & editing, Writing – original draft, Visualization, Investigation. Chaitanya Paramatmuni: Writing – review & editing, Writing – original draft, Validation, Project administration, Conceptualization. Ed Pickering: Writing – review & editing, Supervision, Resources, Project administration. Daniel Cogswell: Supervision, Resources, Project administration, Funding acquisition, Conceptualization.

## Declaration of competing interest

The authors declare that they have no known competing financial interests or personal relationships that could have appeared to influence the work reported in this paper.

#### Acknowledgements

This work was supported by a UKRI Future Leaders Fellowship, United Kingdom [grant number MR/T02058X/1]. The authors would like to thank Steven Hill at WH Tildesley Ltd, Willenhall, United Kingdom, for providing the materials. The authors would also like to extend their gratitude to Ashley Scarlett at the University of Sheffield for reviewing the article.

#### Appendix. Constitutive model parameters

- 1. The parameters in Constitutive Model 1 are presented in Tables A.1 and A.2 and calibrated based on experimental data in the research article by Lin et al. [19], taking into account that  $\alpha = 0.0075 \text{ MPa}^{-1}$ .
- 2. The parameters in Constitutive Model 2 are presented in Tables A.3 and A.4 and calibrated based on experimental data in the research article by Kim et al. [18], taking into account that  $\alpha = 0.0075 \text{ MPa}^{-1}$ .
- 3. The parameters in Constitutive Model 3 are presented in Tables A.5 and A.6 and calibrated based on experimental data in the research article by Venet et al. [20], taking into account that  $\alpha = 0.0075 \text{ MPa}^{-1}$ .

**Table A.1** Calibrated parameters  $Q^*$ ,  $A^*$ ,  $Q_0$  and  $A_0$  in Model 1 at varying strain rates.

Strain rate (s <sup>-1</sup> )	$Q^*$ (J/mol)	$A^*$ (s <sup>-1</sup> )	$Q_0$ (J/mol)	$A_0$ (s <sup>-1</sup> )
0.01	308 115	1.84E+12	237 822	3.91E+10
0.1	324 230	1.23E+13	237 348	1.90E+11
1	323 022	9.78E+12	185 010	2.21E+09
10	329619	1.61E+13	252 033	1.70E+11
50	360 390	2.98E+14	290 232	1.15E+13

**Table A.2** Calibrated parameters  $n^*$  and  $n_0$  in Model 1 at varying temperature.

Temperature (°C)	n*	$n_0$
850	5.73	6.47
950	5.88	7.08
1050	6.24	7.34
1150	6.38	7.22

**Table A.3** Calibrated parameters  $Q^*$ ,  $A^*$ ,  $Q_0$  and  $A_0$  in Model 2 at varying strain rates.

Strain rate (s <sup>-1</sup> )	Q* (J/mol)	$A^*$ (s <sup>-1</sup> )	$Q_0$ (J/mol)	$A_0$ (s <sup>-1</sup> )
0.05	319349	5.55E+12	258 699	1.98E+13
0.5	395 588	9.21E+15	288 867	1.99E+14
5	307 486	1.84E+12	273 783	6.28E+13

**Table A.4** Calibrated parameters  $n^*$  and  $n_0$  in Model 2 at varying temperature.

Temperature (°C)	n*	$n_0$
900	6.03	9.92
1000	5.91	5.98

Table A.5 Calibrated parameters  $Q^*$ ,  $A^*$ ,  $Q_0$  and  $A_0$  in Model 3 at varying strain rates.

Strain rate (s <sup>-1</sup> )	$Q^*$ (J/mol)	$A^*$ (s <sup>-1</sup> )	$Q_0$ (J/mol)	$A_0 (s^{-1})$
0.01	415 148	4.21E+16	650 964	1.10E+30
0.1	354 398	1.60E+14	493 179	3.97E+22
1	396 361	7.99E+15	684871	5.52E+29
10	358 788	2.48E+14	590 096	1.29E+24

Table A.6 Calibrated parameters  $n^*$  and  $n_0$  in Model 3 at varying temperature.

Temperature (°C)	n*	$n_0$
950	5.94	11.12
1000	5.61	8.46
1100	5.96	11.86
1250	5.2	9.77

#### References

- [1] Meysami A, Ghasemzadeh R, Seyedein S, Aboutalebi M. An investigation on the microstructure and mechanical properties of direct-quenched and tempered AISI 4140 steel. Mater Des 2010;31(3):1570-5.
- [2] Bilal MM, Yaqoob K, Zahid MH, Tanveer WH, Wadood A, Ahmed B, et al. Effect of austempering conditions on the microstructure and mechanical properties of AISI 4340 and AISI 4140 steels. J Mater Res Technol 2019;8(6):5194–200.
- [3] Lianggang G, Fengqi W, Pengliang Z, Xuechao L, Mei Z. A novel unified model predicting flow stress and grain size evolutions during hot working of non-uniform as-cast 42CrMo billets. Chin J Aeronaut 2019;32(2):531–45.
- [4] Specification for wrought steel for mechanical and allied engineering purposes Part 3: Bright bars for general engineering purposes. Standard, London, United Kingdom: British Standards Institution; 1991.
- [5] Szala M, Winiarski G, Wójcik Ł, Bulzak T. Effect of annealing time and temperature parameters on the microstructure, hardness, and strain-hardening coefficients of 42CrMo4 steel. Materials 2020;13(9):2022.
- [6] Huang W, Zhong H, Lei L, Fang G. Microstructure and mechanical properties of multi-pass forced and annealed 42CrMo steel. Mater Sci Eng A 2022;831:142191.
- [7] Zhu JG, Sun X, Barber GC, Han X, Qin H. Bainite transformation-kinetics-microstructure characterization of austempered 4140 steel. Metals 2020;10(2):236.

- [8] Quan G-z, Zhao L, Chen T, Wang Y, Mao Y-p, Lv W-q, et al. Identification for the optimal working parameters of as-extruded 42CrMo high-strength steel from a large range of strain, strain rate and temperature. Mater Sci Eng A 2012;538:364–73.
- [9] Mohanty O. Forging grade steels for automotives. In: Automotive steels. Elsevier; 2017, p. 413–53.
- [10] He J. Material 4140 alloy steel: Guide to buy the right material astm-steel.com. 2023, URL https://www.astmsteel.com/steel-knowledge/material-4140-alloy-steel. [Accessed 14 July 2024].
- [11] AISI 4140 chrome-molybdenum high tensile steel azom.com. 2012, URL https://www.azom.com/article.aspx?ArticleID=6116. [Accessed 14 July 2024].
- [12] AISI 4140 A low alloy chromium molybdenum (CrMo) steel. LIBERTY Steel Group, Sheffield, United Kingdom.
- [13] Open die steel forgings for general engineering purposes Part 3: Alloys special steels. Standard, Brussels, Belgium: European Committee for Standardization; 1990
- [14] Chromium Molybdenum Steels JIS G 4105. Standard, Tokyo, Japan: Japanese Standards Association: 1979.
- [15] Zerilli FJ, Armstrong RW. Dislocation-mechanics-based constitutive relations for material dynamics calculations. J Appl Phys 1987;61(5):1816–25. http://dx.doi. org/10.1063/1.338024.
- [16] Johnson GR, Cook WH. A constitutive model and data for metals subjected to large strains, high strain rates and high temperatures. 2018, URL https: //api.semanticscholar.org/CorpusID:211107144.
- [17] Bilbao O, Loizaga I, Alonso J, Girot F, Torregaray A. 42CrMo4 steel flow behavior characterization for high temperature closed dies hot forging in automotive components applications. Heliyon 2023;9(11):e22256. http://dx.doi.org/10.1016/j. heliyon.2023.e22256.
- [18] Kim S, Lee Y, Byon S. Study on constitutive relation of AISI 4140 steel subject to large strain at elevated temperatures. J Mater Process Technol 2003;140(1-3):84-9. http://dx.doi.org/10.1016/s0924-0136(03)00742-8.
- [19] Lin Y, Chen M-S, Zhong J. Effect of temperature and strain rate on the compressive deformation behavior of 42CrMo steel. J Mater Process Technol 2008;205(1–3):308–15. http://dx.doj.org/10.1016/j.jmatprotec.2007.11.113.
- [20] Venet G, Baudouin C, Pondaven C, Bigot R, Balan T. Parameter identification of 42CrMo4 steel hot forging plastic flow behaviour using industrial upsetting presses and finite element simulations. Int J Mater Form 2021;14(5):929–45. http://dx.doi.org/10.1007/s12289-020-01609-1.
- [21] Switzner N, Van Tyne C, Mataya M. Effect of forging strain rate and deformation temperature on the mechanical properties of warm-worked 304L stainless steel. J Mater Process Technol 2010;210(8):998–1007. http://dx.doi.org/10.1016/j. imatprotec.2010.01.014.
- [22] Zhu Z, Lu Y, Xie Q, Li D, Gao N. Mechanical properties and dynamic constitutive model of 42CrMo steel. Mater Des 2017;119:171–9. http://dx.doi.org/10.1016/ j.matdes.2017.01.066.
- [23] Song B, Sanborn B. A modified Johnson–Cook model for dynamic response of metals with an explicit strain- and strain-rate-dependent adiabatic thermosoftening effect. J Dyn Behav Mater 2019;5(3):212–20. http://dx.doi.org/10.1007/ s40870-019-00203-0.
- [24] Steden J, Thimm B. A comprehensive sensitivity analysis of Johnson-Cook plasticity parameters on orthogonal cutting simulations. Procedia CIRP 2021;102:423–8. http://dx.doi.org/10.1016/j.procir.2021.09.072.

- [25] Snape G, Clift S, Bramley A. Parametric sensitivity analyses for FEA of hot steel forging. J Mater Process Technol 2002;125–126:353–60. http://dx.doi.org/10. 1016/s0924-0136(02)00299-6.
- [26] Hill S, Turner RP, Wardle P. The influence of soak temperature and forging lubricant on surface properties of steel forgings. Int J Adv Manuf Technol 2020;112(3-4):1133-44. http://dx.doi.org/10.1007/s00170-020-06468-3.
- [27] Hill S, P.Turner R. Thermo-mechanical forging of 708M40 steel ring samples: experiments and modelling. Int J Adv Manuf Technol 2021;116(7–8):2577–90. http://dx.doi.org/10.1007/s00170-021-07546-w.
- [28] Shen G, Shivpuri R, Semiatin S, Lee J, Altan T. Investigation of microstructure and thermomechanical history in the hammer forging of an Incoloy 901 disk. CIRP Ann 1993;42(1):343-6.
- [29] Weimin C, Bangshun C, Wang Z. A study on the determination of the blow energy of hammers by the steel-column upsetting method. J Mater Process Technol 1995;49(3–4):265–77.
- [30] Galdos L, Sáenz de Argandoña E, Herrero N, Ongay M, Adanez J, Sanchez M. The calibration of high energy-rate impact forging hammers by the coppercolumn upsetting method and high speed camera measurements. Key Eng Mater 2014;611:173–7.
- [31] Collins J, Taylor M, Scarlett A, Palmiere E, Pickering E. Prior austenite grain measurement: A direct comparison of EBSD reconstruction, thermal etching and chemical etching. Mater Charact 2024;208:113656. http://dx.doi.org/10.1016/j. matchar 2024 113656
- [32] SFTC. DEFORM V13.1 MANUAL. 2024, URL https://www.deform.com/.
- [33] Bobzin K, Brögelmann T, Kruppe N, Basturk S, Klocke F, Mattfeld P, et al. Tribological Behavior of (Cr<sub>1-x</sub>Al<sub>x</sub>)N/WS<sub>y</sub> PVD Tool Coatings for the Application in Dry Cold Forging of Steel. Dry Metal Froming Open Access J 2015;1:152–8.
- [34] Medina S, Hernandez C. General expression of the Zener-Hollomon parameter as a function of the chemical composition of low alloy and microalloyed steels. Acta Mater 1996;44(1):137–48. http://dx.doi.org/10.1016/1359-6454(95)00151-0.
- [35] Schindler I, Kawulok P, Kawulok R, Hadasik E, Kuc D. Influence of calculation method on value of activation energy in hot forming. High Temp Mater Processes 2013;32(2):149–55. http://dx.doi.org/10.1515/htmp-2012-0106.
- [36] Razali MK, Joun MS. A new approach of predicting dynamic recrystallization using directly a flow stress model and its application to medium Mn steel. J Mater Res Technol 2021;11:1881–94. http://dx.doi.org/10.1016/j.jmrt.2021.02. 026.
- [37] Lin Y-C, Chen M-S, Zhang J. Modeling of flow stress of 42CrMo steel under hot compression. Mater Sci Eng A 2009;499(1–2):88–92.
- [38] Lin Y, Chen M-S, Zhong J. Numerical simulation for stress/strain distribution and microstructural evolution in 42CrMo steel during hot upsetting process. Comput Mater Sci 2008;43(4):1117–22.
- [39] Chamanfar A, Chentouf S, Jahazi M, Lapierre-Boire L-P. Austenite grain growth and hot deformation behavior in a medium carbon low alloy steel. J Mater Res Technol 2020;9(6):12102–14.
- [40] Ji H, Duan H, Li Y, Li W, Huang X, Pei W, et al. Optimization the working parameters of as-forged 42CrMo steel by constitutive equation-dynamic recrystallization equation and processing maps. J Mater Res Technol 2020;9(4):7210–24.